IEEE Access
Multidisciplinary | Rapid Review | Open Access Journal

Received December 21, 2020, accepted December 31, 2020, date of publication January 5, 2021, date of current version January 13, 2021.

Digital Object Identifier 10.1109/ACCESS.2021.3049252

A Dual Circularly-Polarized Multilayer Reflective Surface Based on Loaded Ring Slots

LOURDES MARTINEZ-LOPEZ, ROSALBA MARTINEZ-LOPEZ, JORGE RODRIGUEZ-CUEVAS, ALEXANDER E. MARTYNYUK, AND JOSE I. MARTINEZ-LOPEZ, (Member, IEEE)
Division de Ingenieria Electrica, Facultad de Ingenieria, Universidad Nacional Autonoma de Mexico, Mexico City 04510, Mexico

Corresponding author: Jose I. Martinez-Lopez (ismartz@unam.mx)

This work was supported in part by the Programa de Apoyo a Proyectos de Investigacion e Innovacion Tecnologica de la Direccion General de Asuntos del Personal Academico (DGAPA PAPIIT) under Grant IN118719, Grant IN118620, and Grant IN119420.

ABSTRACT In this paper, a dual circularly-polarized multilayer reflective surface (MRS) based on loaded ring-slots for reflectarray applications is presented. The MRS comprises a wideband multilayer circular polarizer cascaded with a multilayer reflective screen with independent phase shifting properties for the two orthogonal linearly polarized components. The first polarization conversion is accomplished by a four-layer polarizer based on periodic arrays of bisected split rings that converts two incident circularly-polarized waves, one left-handed (LHCPW) and other right-handed (RHCPW), into two linearly polarized waves with orthogonal polarization planes. These two waves can be phase-shifted independently by a periodic two-layer array of specially designed reflective elements. Each element consists of a ring-slot resonator loaded with two pairs of reactances orthogonally located that can be varied to obtain two linear reflection phase tapers along the array. These reflected waves are then transformed back by the polarizer into two circularly polarized waves traveling into the desired directions. To validate the proposed approach, a six-layer prototype operating at 32 GHz that provides reflection elevation and azimuthal angles for the RHCPW at 22° and 180°, respectively, and reflection elevation and azimuthal angles for the LHCPW at 18° and 0°, respectively, has been designed, fabricated, and experimentally verified.

INDEX TERMS Reflectarrays, circular polarization, ring slot resonators.

I. INTRODUCTION

Nowadays, there is an increasing demand for antenna systems to provide flexibility not only in terms of radiation pattern but also in terms of frequency reconfiguration, polarization-diversity, and multibeam scanning performance. Commonly, phased arrays have been used to provide these multi-function capabilities. However, the high cost in phased array technology prevents their massive use in civil and commercial applications. On the other hand, reflectarray antennas possess most of the main advantages of conventional phased arrays with the benefits of reduced losses, low complexity, and relatively low cost [1]. Recently, reconfigurable reflectarrays have become attractive due to their ability to perform dynamical reconfiguration of the radiation pattern, multibeam scanning, and multi-band operation [2]–[9].

Circular polarized waves (CPW) offer advantages over linearly polarized waves (LPW) such as low multipath interference, low absorption, and insensitivity to the antenna orientation. Therefore, reflectarrays for CPW have become attractive for the research community and various research works have been reported in the past few years [10]–[16]. Several papers have been published dealing with the effort to control the beams independently for the two orthogonal circularly polarized waves. The ability to reconfigure the reflection angles independently for each of the incident circularly polarized waves (right-handed and left-handed) is considered an attractive feature in modern communication systems. The first effort in dealing with this problem was presented in [17], where a multilayer reflectarray based on cranck-shaped $3\lambda/4$ dipoles with dual circularly polarization waves at the same frequency band with independent beam control was introduced. Next, a reflectarray based on a dual surface reflector using a circular polarization selective surface was proposed in [18]. However, the main drawback of this approach is the use of a curved reflector that might represent some challenges in fabrication costs. Later, an approach that provided independent reflection phases for orthogonal CPW was obtained in [19] through a reflectarray unit cell based on a thin polarizer using a modified Jerusalem cross cascaded with

The associate editor coordinating the review of this manuscript and approving it for publication was Weiren Zhu.

a dual linearly polarized reflective patch for multibeam applications. Subsequently, a reflectarray for independent CPW based on stacked Jerusalem crosses was presented in [20]. Afterwards, a reflectarray unit cell based on a thin polarizer using a modified Jerusalem cross cascaded with a dual linearly polarized reflective patch for multibeam space applications was reported in [21]. Next, a two-layer reflectarray cell based on dipoles and arcs that provides circular polarization phase shifting in two different frequencies for multibeam satellite antennas was presented in [22]. A reflectarray using the above-mentioned unit cell has been demonstrated in [23]. Lately, a clever technique that combines the variable size of the element along with the element rotation to obtain a single layer array was proposed in [24]. More recently, a spin-decoupled metasurface for circularly polarized reflector antennas was presented in [25].

Despite the advances obtained in the above-mentioned papers, a higher degree of reconfigurability is necessary in the design of the upcoming new generation of wireless communication systems. Therefore, the possibility to reconfigure each single unit cell based on varying the loading in the ring slot resonators to offer distinct reflection phases, and the study of the super cells that can be obtained to offer linear phase tapers are explored in this work with the aim to provide polarization diversity along with beam scanning properties.

The proposed approach offers independent control of the reflection coefficient phase for each of the orthogonal circularly polarized components of the incident wave by means of properly adjusting the reactive loading of the ring slots. In this paper, a multilayer reflective surface (MRS) that forms two independent lobes for two orthogonally polarized CPWs is studied. The validation of the proposed MRS is achieved by the characterization of a frozen prototype. The various values of reactive loads are replaced by metal patches with different lengths. The proposed MRS approach can be used as a proof of concept for designing reconfigurable reflectarrays with enhanced flexibility in terms of polarization diversity and beamforming capabilities.

II. PRINCIPLE OF OPERATION

The proposed MRS consists of a cascaded connection of two main blocks as shown in Fig. 1(a). The first block is a wideband multilayer circular polarizer (WCP) and the second block is an array of reflective phase shifting elements with integrated phase shifters. The WCP block is built as a four-layer array of bisected split rings and has been previously designed and described in [26]. The geometry of the WCP unit cell is shown in Fig. 1(b). The second block consists of a two-layer array based on ring slot resonators loaded by variable reactances X_u and X_w, as depicted in Fig. 1(c) and backed with a metal screen situated at a fixed distance. The WCP elements as well as the loaded resonators are located at the nodes of a square grid with period b.

The operation of the MRS is as follows. Suppose that a normally incident left-handed circularly polarized wave (LHCPW) illuminates the surface. After passing

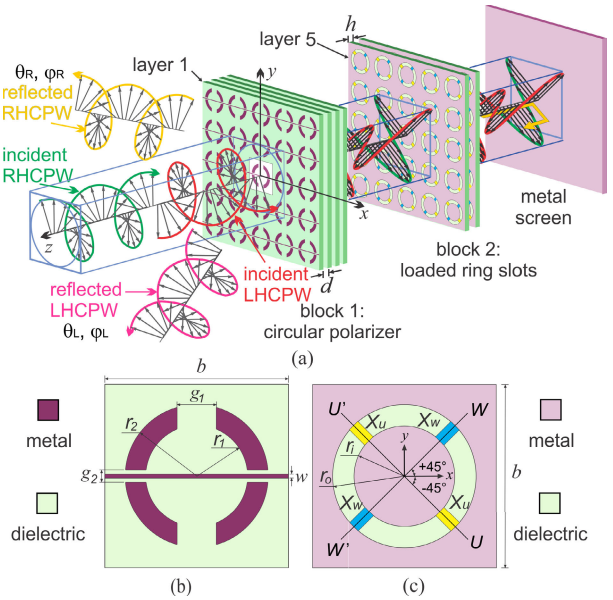

FIGURE 1. (a) Dual polarized reflective surface for circularly polarized waves, (b) geometry of the circular polarized unit cell, and (c) geometry of the phase shifting section.

through block 1, this LHCPW is transformed into a linearly polarized wave (LPW) with electric field vector positioned at $-45°$ to the x-axis (parallel to the axis U-U'). In block 2, this electric field vector is parallel to the reactances X_u. On the other hand, if the incident polarized wave is right-handed (RHCPW), the exiting LPW from block 1 has an electric field vector oriented at $+45°$ to the x-axis (parallel to the axis W-W'), being parallel to the reactances X_w. It is important to point out the orthogonality of axes U-U' and W-W', as the transformed linearly polarized waves (one parallel to -45° axis and other parallel to $+45°$ axis), will be experiencing different loading conditions through the loads X_u and X_w, respectively. Now consider that a normally-incident CPW illuminates the surface with all elements having the same reactance values, this uniform loading ensures that the reflected CPW will travel in the broadside direction. However, if the contiguous elements along any of the coordinate axes are loaded with different reactance values, it is possible to introduce a linear phase taper along that coordinate axis. The nonuniform loading of the elements allows one to redirect the reflected CPW into a required direction.

To independently reflect the normally-incident RHCPW and LHCPW in the directions respectively defined by the reflection elevation angles θ_R and θ_L, and the reflection azimuthal angles ϕ_R and ϕ_L, the adjacent cells must provide incremental or decremental phase shifts of ψ_{Rx} and ψ_{Lx} in the x direction, and ψ_{Ry} and ψ_{Ly} in the y direction. These phase shifts can be calculated as:

$$\begin{aligned}
\psi_{Rx} &= -kb\sin\theta_R\cos\varphi_R,\\
\psi_{Ry} &= -kb\sin\theta_R\sin\varphi_R,\\
\psi_{Lx} &= -kb\sin\theta_L\cos\varphi_L,\\
\psi_{Ly} &= -kb\sin\theta_L\sin\varphi_L,
\end{aligned} \tag{1}$$

where k is the wavenumber.

For a special case, the required incremental phase shifts established by (1) can be approximated as a multiplication of a rational number by 2π:

$$\begin{aligned}\psi_{Rx} &= \frac{M_{Rx}}{N_{Rx}}2\pi,\\ \psi_{Ry} &= \frac{M_{Ry}}{N_{Ry}}2\pi,\\ \psi_{Lx} &= \frac{M_{Lx}}{N_{Lx}}2\pi,\\ \psi_{Ly} &= \frac{M_{Ly}}{N_{Ly}}2\pi,\end{aligned} \tag{2}$$

where N_{Rx}, N_{Ry}, N_{Lx}, N_{Ly} are positive integer numbers and M_{Rx}, M_{Ry}, M_{Lx}, M_{Ly} are integer numbers with absolute values less than $N_{Rx}/2$, $N_{Ry}/2$, $N_{Lx}/2$, and $N_{Ly}/2$, respectively, to avoid phase ambiguity. Thus, two rectangular super cells (*R-cell* and *L-cell*) containing $N_{Rx}N_{Ry}$ and $N_{Lx}N_{Ly}$ elements, respectively, are formed for the incident RHCPW and LHCPW. Indeed, these two different super cells, one for the case of the RHCPW and other for the LHCPW, can redirect each of the reflected CPW into a desired direction. The pair of reactances in each ring slot resonator (X_{ui} and X_{wi}) within the super cells can be controlled independently and they ensure the proper phase of the reflection coefficient, where i is the index that define the location of the single cell within the super cell.

For the case of the incident RHCPW, phase shift variations of $M_{Rx}2\pi$ and $M_{Ry}2\pi$ are ensured along the R-cell in the x- and y- directions, respectively. On the other hand, L-cell provides total phase shifts of $M_{Lx}2\pi$ and $M_{Ly}2\pi$ along the x and y axis, respectively. Thus, the independent control of the reflection angles for the normally-incident LHCPW and RHCPW is produced in the MRS.

By merging R-cell and L-cell together, an infinite periodic reflective structure is formed with a rectangular periodic megasupercell containing $N_{Tx} = N_{Rx}N_{Lx}/N_{cx}$ elements in x-direction and $N_{Ty} = N_{Ry}N_{Ly}/N_{cy}$ elements in y- direction, where N_{cx} is the largest common factor of N_{Rx} and N_{Lx}, meanwhile N_{cy} is the largest common factor of N_{Ry} and N_{Ly}.

According to Floquet's theorem, the electromagnetic field at $z = 0$ within the megasupercell can be presented a sum of *TE* Floquet modes $\vec{\Psi}_{1mn}$ and *TM* Floquet modes $\vec{\Psi}_{2mn}$ [27]:

$$\begin{aligned}\vec{\Psi}_{1mn} &= \sqrt{\frac{1}{N_{Tx}N_{Ty}b^2}}\left[\frac{k_{yn}\vec{a}_x - k_{xm}\vec{a}_y}{k_{rmn}}\right]e^{-j(k_{xm}x+k_{yn}y)},\\ \vec{\Psi}_{2mn} &= \sqrt{\frac{1}{N_{Tx}N_{Ty}b^2}}\left[\frac{k_{yn}\vec{a}_x + k_{xm}\vec{a}_y}{k_{rmn}}\right]e^{-j(k_{xm}x+k_{yn}y)},\end{aligned} \tag{3}$$

where $k_{xm} = 2\pi m/N_{Tx}b$ and $k_{yn} = 2\pi n/N_{Ty}b$ are the x- and y- components, respectively, of the wavenumber vector $\vec{k}$ of magnitude k; m and n are integer numbers; $k_{rmn} = \sqrt{k_{xm}^2 + k_{yn}^2}$ is the transverse component of $\vec{k}$; $\vec{a}_x$ and $\vec{a}_y$ are the unit vectors in the x- and y- directions, respectively, and $j = \sqrt{-1}$.

From the physical point of view, these *TE* and *TM* Floquet modes are *TE* and *TM* plane waves that propagate or decay along the z- axis according to $\exp(\pm j\Gamma_{mn}z)$, the z- component of the wavenumber vector is calculated as:

$$\Gamma_{mn} = \sqrt{k^2 - k_{xm}^2 - k_{yn}^2}. \tag{4}$$

Due to the considerable electrical size of the megasupercell, many Floquet modes are reflected plane waves propagating in different directions from the array. Therefore, the electric field above the MRS can be presented as:

$$\begin{aligned}\vec{E} = &\left[A_0^R\left(\vec{\Psi}_{1,0,0} + j\vec{\Psi}_{2,0,0}\right) + A_0^L\left(\vec{\Psi}_{1,0,0} - j\vec{\Psi}_{2,0,0}\right)\right]e^{jkz}\\ &+\sum_{p=1}^{2}\sum_{m=-\infty}^{\infty}\sum_{n=-\infty}^{\infty}R_{pmn}\vec{\Psi}_{pmn}e^{-j\Gamma_{mn}z},\end{aligned} \tag{5}$$

where A_0^R and A_0^L are the complex magnitudes of the normally-incident RHCPW and LHCPW, respectively, and R_{pmn} is the complex magnitude of the reflected Floquet mode $\vec{\Psi}_{pmn}$.

The first term of (5) contains the normally incident circularly polarized waves propagating towards the MRS, while the infinite sum includes the reflected plane waves.

After passing back through the polarization converter, the two orthogonal linearly polarized waves are converted into circularly polarized waves. Two of the reflected Floquet modes (one *TE* and one *TM*) will be propagating into the direction determined by (θ_R, φ_R), while other two reflected Floquet modes will be traveling to the direction defined by (θ_L, φ_L). Therefore, each incident CPW is converted into a reflected CPW with the same polarization according with the phase taper defined by (1). The rest of the Floquet modes are either evanescent or they will be plane waves traveling into undesired directions, therefore it is important to obtain the efficiencies of the wave transformations. The efficiencies of theses modal conversions are calculated as the ratio between the power density of the Floquet modes traveling in the desired direction and the power density of the normally-incident CPW. These conversion coefficients are given by:

$$\begin{aligned}L_R &= \frac{Y_{1,m1,n1}\left|R_{1,m1,n1}\right|^2 + Y_{2,m1,n1}\left|R_{2,m1,n1}\right|^2}{2Y_{1,0,0}\left|A_0^R\right|^2},\\ L_L &= \frac{Y_{1,m2,n2}\left|R_{1,m2,n2}\right|^2 + Y_{2,m2,n2}\left|R_{2,m2,n2}\right|^2}{2Y_{1,0,0}\left|A_0^L\right|^2},\end{aligned} \tag{6}$$

where Y_{pmn} is the Floquet modal admittance of $\vec{\Psi}_{pmn}$; $\vec{\Psi}_{1,m1,n1}$ and $\vec{\Psi}_{2,m1,n1}$ are the Floquet modes traveling in the direction (θ_R, φ_R), and $\vec{\Psi}_{1,m2,n2}$ and $\vec{\Psi}_{2,m2,n2}$ are the Floquet modes traveling in the direction (θ_L, φ_L).

To illustrate the periodicities of the two super cells, Fig. 2 shows a section of one reflective surface containing two super cells: one cell of 4×3 elements for the LHCPW (shaded red) and one cell of 3×4 elements for the RHCPW (shaded blue). The parameters of the super cell for the LHCPW are given by $N_{Lx} = 4$, $N_{Ly} = 3$, $M_{Lx} = 1$, $M_{Ly} = 1$, $\psi_{Lx} = 90°$,

and $\psi_{Ly} = 120°$, while for the super cell of the RHCPW are $N_{Rx} = 3$, $N_{Ry} = 4$, $M_{Rx} = -1$, $M_{Ry} = 1$, $\psi_{Rx} = -120°$, and $\psi_{Ry} = 90°$. For this case, an infinite periodic structure with a square megasupercell that contains 12×12 reflectarray elements is formed. The required incremental or decremental phase shifts values in the x- or y- directions can be obtained by properly setting the values of the reactive loads X_{ui} and X_{wi} in each ring slot resonator within the corresponding super cell. The reflected LPWs are then converted into CPWs after traveling through block 1 in the positive z- direction of the array preserving the phase gradients obtained by block 2, ensuring the desired directions for the reflected CPWs.

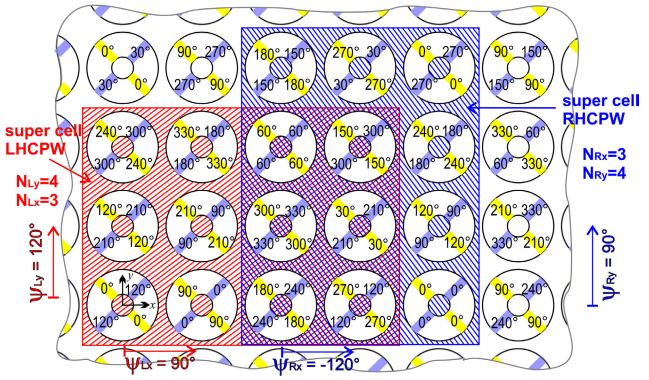

FIGURE 2. Section of the MRS containing two super cells with $N_{Lx} = 4$, $N_{Ly} = 3$, $M_{Lx} = 1$, $M_{Ly} = 1$, $\psi_{Lx} = 90°$ and $\psi_{Ly} = 120°$ for the LHCPW, and $N_{Rx} = 3$, $N_{Ry} = 4$, $M_{Rx} = -1$, $M_{Ry} = 1$, $\psi_{Rx} = -120°$ and $\psi_{Ry} = 90°$ for the RHCPW.

III. REFLECTIVE MULTILAYER SCREEN DESIGN

A reflective surface operating at 32 GHz was designed to evaluate the afore-mentioned operation principle. In this paper, the beam scanning with ϕ_R equal to 180° and ϕ_L equal to 0° are analyzed, however, the scanning for ϕ_R and ϕ_L different from these angles can also be achieved with this approach. Initially, the array element of the two-layer array presented in block 2 of Fig. 1(a) is designed. The goal is to obtain an element that provides a phase shift with low insertion loss. The mechanism to obtain the phase shift is to change the value of the reactive loading. This array element comprises a ring-slot resonator with inner radius r_i and outer radius r_o loaded with four reactive loads located at 45°, 135°, 225° and 315° from the x- axis. The sizes of the analyzed unit cell are given by $r_i = 1.19$ mm, $r_o = 2.19$ mm, and $b = 5$ mm. A microwave laminate with relative permittivity εr of 2.2, loss tangent of 0.0009, dielectric thickness h of 0.127 mm, and copper cladding thickness h_c of 12 μm was considered in the design. The space between layers was initially set to 2 mm.

A. EQUIVALENT CIRCUIT MODEL

To facilitate the design and synthesis of the unit cell geometry, an equivalent circuit model (ECM) is proposed for the two-layer structure and the metal screen. Fig. 3(a)-(b) show the ECMs viewed from the two auxiliary axes *U-U'* and *W-W'*, where L is the inductance due to the electric currents that flow along the metal part of the ring resonators and C is the capacitance due to the electric field stored at the ring slot aperture. Transmission line TL_{sus} models the dielectric substrate, and TL models the free space between layers, and X_u and X_w are the values of the reactive loads parallel to the axes *U-U'* and *W-W'*, respectively. The metal screen is modeled by a short circuit. With these ECMs, one can obtain the required values of reactive loads to achieve different phase shifts of the reflected waves.

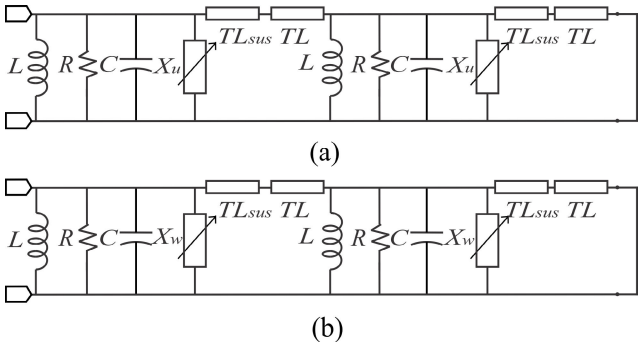

FIGURE 3. Equivalent circuit models of the two-layer reflective array for (a) linear polarized wave converted from the LHCPW, and (b) linear polarized wave converted from the RHCPW.

The scattering of a linearly polarized wave from the unloaded ring slots was simulated to obtain the reflection coefficients and the reference reflection phase ψ_0. At 32 GHz, the component values of the ECM for the unloaded ring slots were obtained by approximating the response of the ECM to the one obtained with a full-wave method. The component values are given by $C = 29.9$ fF, $L = 0.793$ nH, $R = 171.7$ kΩ, TL_{sus} with a characteristic impedance $Z_{0\_SUS} = 254.2$ Ω and electrical length E_{SUS} of 7.2°, and TL with $Z_0 = 377$ Ω and $E = 72°$. In the following step, the effect of adding the reactive capacitive loads to the ring-slot for obtaining different reflection phases is analyzed.

In this design, we intend to reflect two normally-incident circularly-polarized plane waves, one left-handed and other right-handed, to different directions determined by reflection angles determined by (θ_L, ϕ_L) and (θ_R, ϕ_R), respectively. To demonstrate this possibility of such redirection, a 6 × 1-element supercell ($SC6\times1$) and a 5 × 1-element supercell ($SC5\times1$) have been considered for the LHCPW and RHCPW, respectively.

According to (2), the $SC6 \times 1$ ($N_{Lx} = 6$, $N_{Ly} = 1$) potentially provides incremental phase shifts ψ_{Lx} of ±120° ($M_{Lx} = \pm2$), ±60° ($M_{Lx} = \pm1$), or 0° ($M_{Lx} = 0$) as well as $\psi_{Ly} = 0°$ ($M_{Ly} = 0$). On the other hand, the $SC5\times1$ ($N_{Rx} = 5$, $N_{Ry} = 1$) ensures ψ_{Rx} of ±144° ($M_{Rx} = \pm2$), ±72°($M_{Rx} = \pm1$) or 0° ($M_{Rx} = 0$) together with $\psi_{Ry} = 0°$ ($M_{Ry} = 0$). Zero values of ψ_{Ly} and ψ_{Ry} lead to a simplification of (1). For this case, the substitution of (2) in (1) permits to

calculate the reflection angles as follows:

$$\theta_R = \sin^{-1}\left|\frac{\lambda}{b}\frac{M_{Rx}}{N_{Rx}}\right|,$$
$$\varphi_R = \begin{cases} 0, & \text{for } M_{Rx} \le 0 \\ \pi, & \text{for } M_{Rx} > 0 \end{cases},$$
$$\theta_L = \sin^{-1}\left|\frac{\lambda}{b}\frac{M_{Lx}}{N_{Lx}}\right|,$$
$$\varphi_L = \begin{cases} 0, & \text{for } M_{Lx} \le 0 \\ \pi, & \text{for } M_{Lx} > 0 \end{cases}, \quad (7)$$

where λ is free-space wavelength.

Thus, at 32 GHz and considering $b = 5$mm, the properly configured *SC6×1* provides θ_L equal to $\pm 18.2°$ ($M_{Lx} = \mp 1$), $\pm 38.7°$ ($M_{Lx} = \mp 2$) or $0°$ ($M_{Lx} = 0$). Consequently, the properly configured *SC5×1* ensures θ_R equal to $\pm 22°$ ($M_{Rx} = \mp 1$), $\pm 48.6°$ ($M_{Rx} = \mp 2$) or $0°$ ($M_{Rx} = 0$).

To demonstrate an operation principle, the *SC5×1* has been optimized for the case of $M_{Rx} = 1$, $M_{Ry} = 0$, $\psi_{Rx} = 72°$, and $\psi_{Ry} = 0°$ to reflect the normally-incident RHCPW in the direction (22°,180°), meanwhile the *SC6×1* has been configured for $M_{Lx} = -1, M_{Ly} = 0$, $\psi_{Lx} = -60°$, and $\psi_{Ly} = 0°$ to redirect the normally-incident LHCPW in the direction (18.2°,0°).

It should be useful to mention that the *SC5×1* converts the superposition of the normally-incident $\vec{\Psi}_{1,0,0}$ and $\vec{\Psi}_{2,0,0}$ modes that form the incident RHCPW into the reflected Floquet modes $\vec{\Psi}_{1,-1,0}$ and $\vec{\Psi}_{2,-1,0}$ traveling in the direction (22°,180°). Similarly, the *SC6×1* converts the superposition of the normally-incident $\vec{\Psi}_{1,0,0}$ and $\vec{\Psi}_{2,0,0}$ modes that form the incident LHCPW into the reflected Floquet modes $\vec{\Psi}_{1,1,0}$ and $\vec{\Psi}_{2,1,0}$ traveling in the direction (18.2°,0°). Consequently, reflection phases of (0°, -60°, -120°, -180°, -240°, and -300°) and (0°, -288°, -216°, -144°, and -72°) need to be obtained with the loading capacitors.

The required load capacitances to accomplish the reactive loads $X_u = -1/(2\pi f C_i)$ and $X_w = -1/(2\pi f C_j)$ for achieving the targeted phase shifts can be obtained with the help of the ECMs. The capacitance values of the loads to obtain the required phase shifts are shown in Table 1, where ψ_0 is the initial reference phase shift of the unload ring-slot.

The calculated phases and magnitudes of the reflection coefficients with the help of Keysight ADS are shown in Fig. 4(a) and (b), respectively. The phases obtained for capacitors C_1 to C_9 are plotted subtracting the reference phase ($\psi_i - \psi_0$). It is observed low insertion loss for the required phases at 32 GHz.

B. REACTIVE LOAD IMPLEMENTATION USING METAL PATCHES

The loading capacitors within the ring-slots can be implemented using metal patches *MP*. To build these loading capacitances, a metal patch with length l_s and width w_s is connected into the ring slot as shown in Fig. 5. This metal patch can modify the capacitance of the slot by changing

TABLE 1. Phase shifts obtained due to the loading capacitors.

Capacitor	Phase shift	Loading capacitor [fF]
C_0	Ψ_0	0
C_1	Ψ_0-60°	7.09
C_2	Ψ_0-72°	8.45
C_3	Ψ_0-120°	12.5
C_4	Ψ_0-144°	13.9
C_5	Ψ_0-180°	15.8
C_6	Ψ_0-216°	17.5
C_7	Ψ_0-240°	18.7
C_8	Ψ_0-288°	21.9
C_9	Ψ_0-300°	23.0

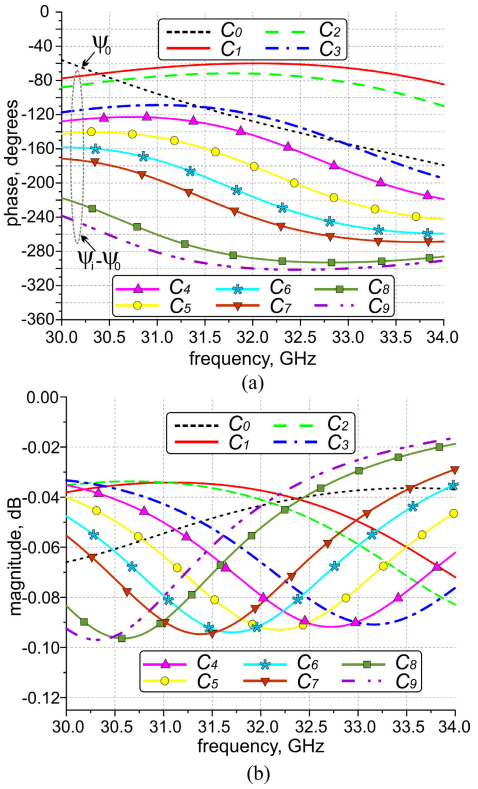

FIGURE 4. Reflection coefficient calculated with the ECM model vs. frequency (a) phase and (b) magnitude.

the gap of the ring slot at the location of the load. In other words, by increasing the length of the metal patch, the gap reduces, increasing the electric field stored in the aperture and thus the value of the load capacitance also increases. The lengths ls_i of the metal patches can be adjusted to obtain the required phase taper at the designed frequency. A width w_s of 0.42 mm is considered for all calculations. Fig. 5 shows the phase and magnitude of the reflection coefficient in terms of the length l_s of the metal patch. Then, nine metal patches MP_1-MP_9 with their correspondent lengths are used to implement the capacitors C_1-C_9.

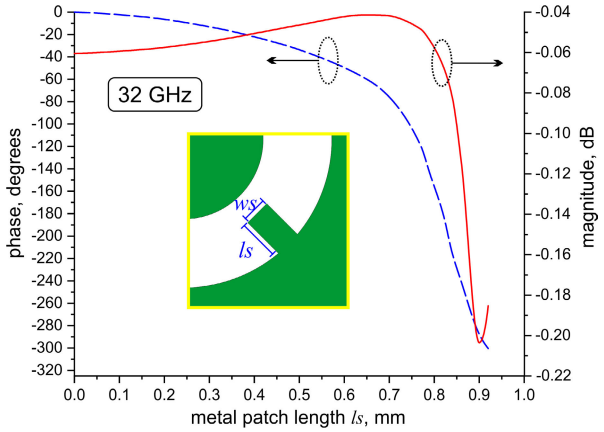

FIGURE 5. Reflection coefficient phase and magnitude of the ring slot loaded with metal patches vs. patch length *ls*.

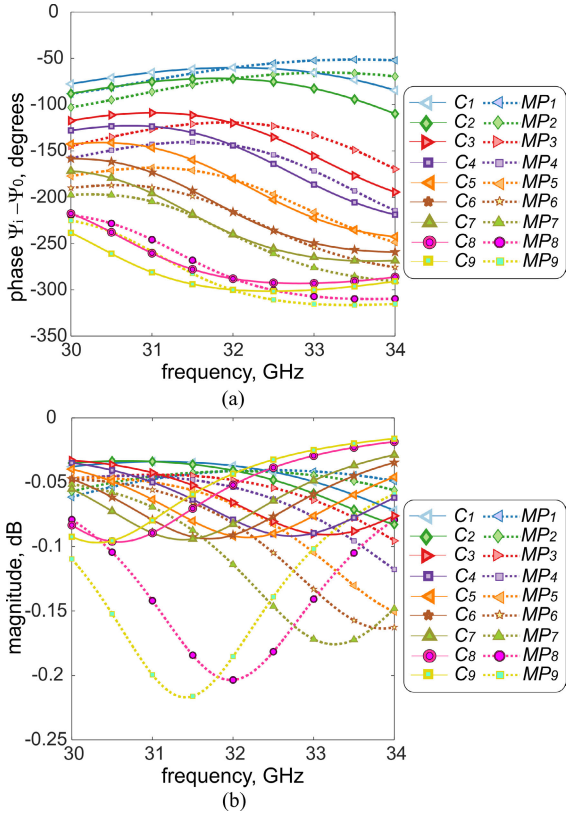

FIGURE 6. Comparison of the reflection coefficient calculated from the ECM and the single unit cell of block 2, (a) reflected phase and (b) magnitude.

The comparison of the reflection coefficient obtained from the ECMs and the ones obtained from the single unit cell of block 2 using a full-wave solver is presented in Fig. 6. Fig. 6(a) shows the reflected phases $\psi_i - \psi_0$ and Fig. 6(b) shows the reflection coefficient magnitudes. At 32 GHz, a close agreement in the reflected phases is observed, while acceptable phase differences are found at nearby frequencies. On the other hand, simulated reflection loss found for block 2 is lower than 0.22 dB, which is also acceptable for reflectarray applications.

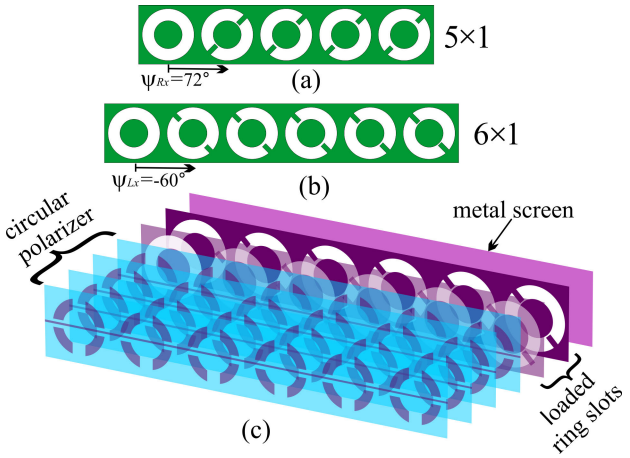

FIGURE 7. Super cells configuration. (a) 5 × 1 element super cell for RHCPW, (b) 6 × 1 element super cell for LHCPW, and (c) 6 × 1 element super cell of the MRS for the LHCPW.

The super cells *SC5*×1 and *SC6*×1 for the cases of 5 × 1 and 6 × 1 elements are shown in Fig. 7(a) and (b) for the RHCP and LHCP, respectively. These configurations ensure the beam scanning in the *XOZ* plane. Fig. 7(c) shows the complete periodic super cell for the *SC6*×*1* case including the multilayer circular polarizer. A previously designed circular polarization converter reported in [26] was considered in layers 1-4. The sizes of the circular polarizer are given by $r_1 = 1.2$ mm, $r_2 = 1.9$ mm, and $g_1 = 1$ mm for layers 1 and 4, while for layers 2 and 3 are given by $r_1 = 1.5$ mm, $r_2 = 2.2$ mm, and $g_1 = 2$ mm. The sizes $g_2 = 0.5$ mm and $w = 0.1$ mm are the same for all layers.

The MRS was analyzed as an infinite periodic array using Floquet's theorem. The distances between layers were optimized to ensure low conversion loss of the modal transformation. The distances between the circular polarizer layers are 2.5 mm, while the distances between the loaded ring slot arrays and the metal screen are 2.0 mm. These optimizations were performed with the help of a full-wave frequency domain solver within CST Studio Suite using boundary conditions of the unit cell. The magnitudes of the propagating Floquet modes for the *SC5*×*1* are shown in Fig. 8, one can observe that the two modes with the larger magnitudes correspond to the plane waves traveling into the desired directions.

The computed conversion coefficients for the *SC*5 × 1 and *SC*6 × 1 are shown in Fig. 9. From the simulated results, it is observed low conversion losses near the targeted frequency for both components that ensure the adequate modal conversion of the incident CPWs. In the same Fig. 9, the conversion coefficients for super cells of 3 × 1, 4 × 1, 7 × 1, and 8 × 1 element along the *x*- axis are also shown. The necessary incremental phase shifts between elements for these super cells are 120°, 90°, 51.43°, and 45° for the 3 × 1, 4 × 1, 7 × 1, and 8 × 1, respectively. The required lengths of the metal patches to get all these phase shifts were also obtained according to the relations shown in Fig. 5.

Finally, a medium size MRS with 19 × 19 elements containing the circular polarizer, the two-layer loaded ring slot

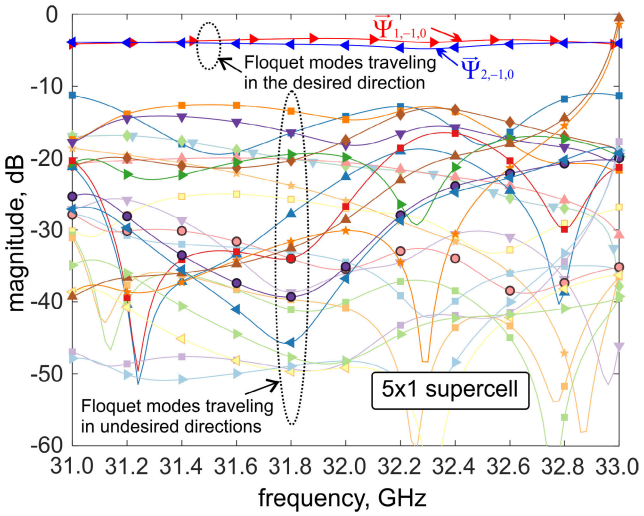

FIGURE 8. Magnitudes of the propagating Floquet modes for SC5 × 1.

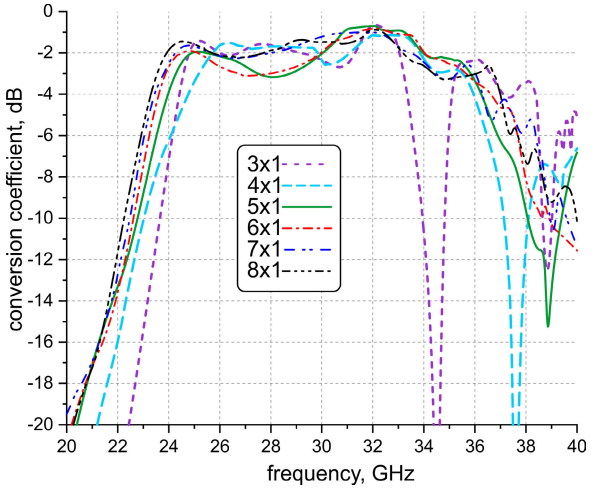

FIGURE 9. Simulated conversion coefficient of different super cells.

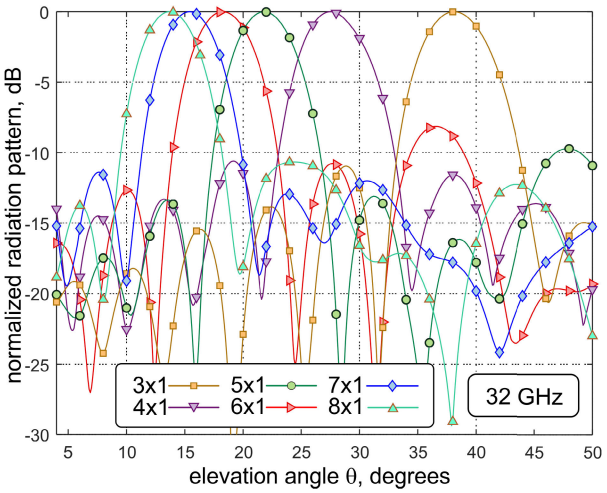

FIGURE 10. Simulated radiation patterns for a 19 × 19 -element array with different super cells at 32 GHz.

reflective surface, and the metal screen was simulated in the time domain solver within CST Studio Suite to calculate the radiation patterns of the different super cells. A right-hand and a left-hand circularly polarized plane waves were used as excitations of the MRS and a farfield monitor at 32 GHz was employed to plot the radiation pattern. Boundary conditions were set as open add space in $-x$, $+x$, $-y$, $+y$ and $+z$ directions.

Fig. 10 shows the normalized radiation patterns at 32 GHz for a 19 × 19 -element array with super cells of 3 × 1, 4 × 1, 5 × 1, 6 × 1, 7 × 1, and 8 × 1 -elements along the x- axis. It is observed that the main beam is oriented at the reflection elevation angles of 39°, 28°, 22°, 18°, 16°, and 14°, respectively.

IV. REFLECTIVE SCREEN FABRICATON AND CHARACTERIZATION

A. MRS FABRICATION

A 361-element array prototype (19 × 19 elements) to validate the simulated results was fabricated and tested. The reflective surface demonstrator fabricated in this paper contains two super cells, the first one $SC5\times1$ with $N_{Rx} = 5$, $N_{Ry} = 1$, $M_{Rx} = 1$, and $M_{Ry} = 0$ to provide phase shifts of $\psi_{Rx} = 72°$ and $\psi_{Ry} = 0°$, and the second one $SC6\times1$ with $N_{Lx} = 6$ and $N_{Ly} = 1$, $M_{Lx} = -1$, and $M_{Ly} = 0$ to offer phase shifts of $\psi_{Lx} = -60°$ and $\psi_{Ly} = 0°$. For the 5×1-element super cell it was defined an incremental phase shift to obtain a reflection elevation angle for the RHCPW with $\phi_R = 180°$, while for the 6 × 1 element super cell it was chosen a decremental phase shift to obtain a reflection elevation angle with $\phi_L = 0°$. According to (1), these phase shifts can provide reflection elevation angles of $\theta_R = 22.0°$ and $\phi_R = 180°$ for the RHCPW, and $\theta_L = 18.2°$ and $\phi_L = 0°$ for the LHCPW, respectively.

The elements of the MRS were formed on the microwave-friendly laminate Rogers 5880 with $\varepsilon_r = 2.2$, tan $\delta = 0.0009$, $h = 0.127$ mm, and h_c of 17 μm, using a standard photolithography process. To minimize fabrication errors, the copper cladding thickness was reduced to 12 μm before etching the element features to avoid undercutting. To ensure the correct distance between layers, frames acting as spacers made from acrylic glass were used. A photograph of the first six cells in x- direction is shown in 11(a), indicating the phase shifts obtained with the reactive loading for the $SC5\times1$ and $SC6$ × 1. These phase shifts were obtained according to (1) and (2). The assembled surfaces comprising block 2 are shown in Fig. 11(b), while the complete MRS is shown in Fig. 11(c). Special care was taken to accurately line up all the layers to minimize misalignment errors.

B. MRS CHARACTERIZATION

A measurement setup was used to obtain the radiation characteristics of the fabricated MRS in free space. A vector network analyzer connected to two corrugated scalar horns acting as transmitting and receiving antennas were used to characterize the MRS. A rectangular to circular wave transition was used to convert the TE_{10} mode in the rectangular waveguide to the

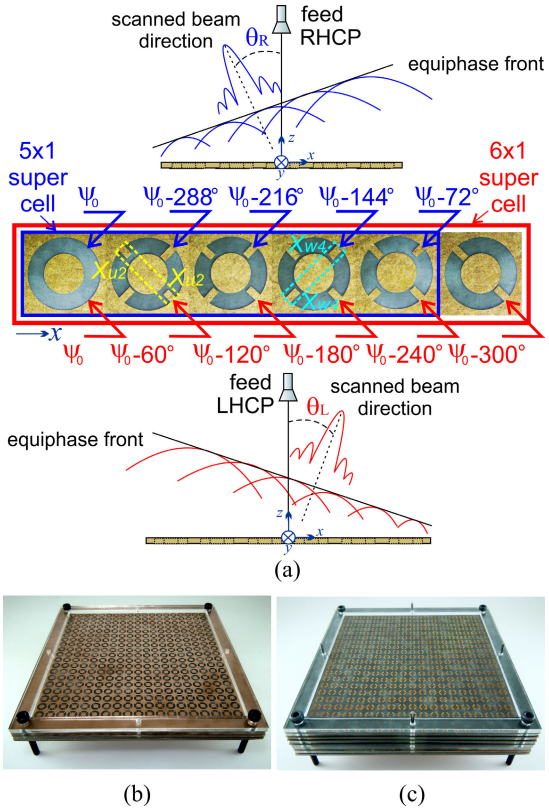

FIGURE 11. Photographs of the fabricated prototypes (a) first six cells from left to right indicating the phase shifts obtained with the reactive loading for the SC5 × 1 and SC6 × 1, (b) two-layer 361-element phase shifting loaded ring slot surfaces, and (c) complete six-layer 361-element MRS.

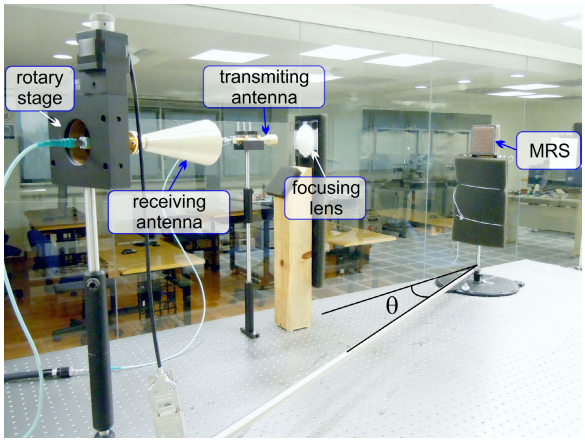

FIGURE 12. Free space measurement setup.

TE_{11} mode in the circular waveguide. The transmitting horn antenna with a wideband circular polarizer was positioned at broadside direction while the receiving horn antenna was situated at various reflection elevation angles to obtain the array's radiation pattern. A focusing dielectric lens was used to obtain a quasi-plane wave that propagates towards the MRS. A stepper motor rotary stage was used at the receiving antenna to measure the polarization ellipse of the incoming electromagnetic wave. A diagram of the measured setup is shown in Fig. 12.

The measured and simulated radiation patterns for the incident RHCPW and LHCPW at 32 GHz are presented in Fig. 13(a) and (b), respectively. The simulated results were obtained analyzing the medium size 19 × 19 element MRS in the time domain with the help of CST Studio Suite and the measured results were obtained with the free-space measurement setup. The blue and the red solid lines were obtained illuminating the MRS with quasi-plane normally-incident RHCPW and LHCPW, respectively, while the blue and the red dashed lines were simulated using plane normally-incident RHCPW and LHCPW, respectively. The measured and simulated angular dependence of the axial ratios at 32 GHz for the RHCPW and LHCPW are shown in Fig. 14(a) and (b), respectively, while the measured and simulated frequency dependence of the axial rations at $\theta_R = 22.0°$ and $\theta_L = 18°$ are shown in Fig. 14(c) and (d), respectively.

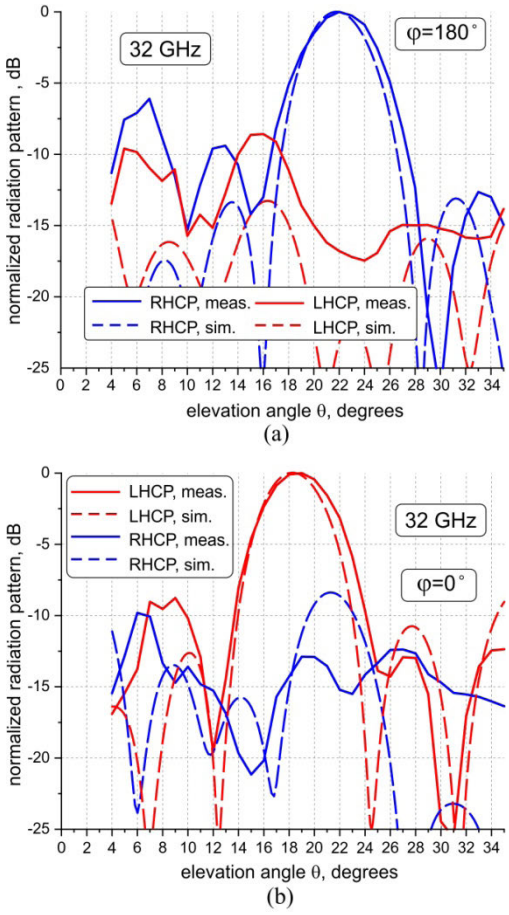

FIGURE 13. Measured and simulated radiation pattern of the fabricated array at 32 GHz, (a) main beam of RHCPW ($\phi_R = 180°$), (b) main beam of LHCPW ($\phi_L = 0°$).

From the measured results it is observed that the RHCPW and the LHCPW are reflected in the opposite directions from *YOZ* plane and agree well with the theory predicted at 22.0° ($\phi_R = 180°$) and 18° ($\phi_L = 0°$), respectively. With the uniform illumination of the finite-size prototype, the delta-function that corresponds to the Floquet modes traveling into

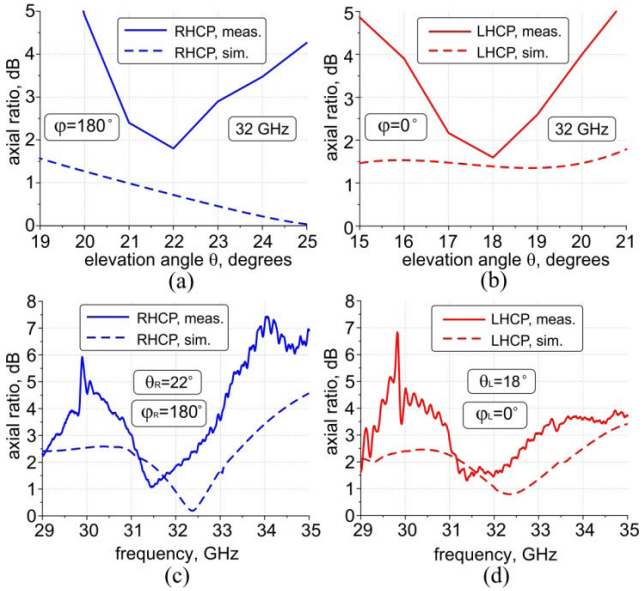

FIGURE 14. **Measured and simulated angular dependence of the axial ratio at 32 GHz for (a) RHCPW, and (b) LHCPW, and measured and simulated frequency dependence of the axial ratio for (c) RHCPW ($\theta_R = 22.0°$, $\phi_R = 180°$), and (d) LHCPW ($\theta_L = 18.0°$, $\phi_L = 0°$).**

the desired direction is converted into the main lobe with a beamwidth of $51° \cdot \lambda/(L \cdot \cos(\theta_0))$, where L is the length and height of the square prototype. The estimated beamwidth value of 5.4° agrees well with the simulated value of 5.5° and the measured value of 6°. The relatively high side lobe levels (SLL) observed can be explained from the uniform illumination of the MRS, phase errors at the MRS border, and the partial conversion of the incident CPW to the waves traveling into undesired directions. Also, these SLL are not symmetric and are higher near the broadside direction due to the obstructive profile of the transmitting horn antenna rod in the measurement setup. The measured transmission loss of the circular polarizer at 32 GHz is 0.45 dB, therefore by passing twice the aggregate insertion loss is 0.9 dB. The conversion loss of the phase-shifting section at 32 GHz is 0.36 dB for the RHCPW, and 0.59 dB for the LHCPW. Therefore, the total conversion loss is estimated at 1.26 dB for the RHCPW, and 1.49 dB for the LHCPW. Furthermore, axial ratios were lower than 3 dB from 31.01 to 32.69 GHz for the reflected RHCPW, and from 30.98 to 32.91 GHz for the reflected LHCPW.

V. CONCLUSION

A multilayer dual circular-polarized reflective surface based on loaded ring slot resonators has been investigated in this paper. The conversion of two circularly polarized normally incident plane waves into two linearly polarized waves with orthogonal polarization planes that can be independently phase shifted by ring slots with two different pairs of capacitive loads located at their two orthogonal axes was studied in this paper. Two super cells were analyzed and modeled to design the MRS. The variation of the loading reactances allows one to define the required phase tapers to steer the two beams into different reflection elevation angles. A demonstrator with frozen loads to operate at 32 GHz, with different reflection elevation angles for the RHCPW and LHCPW was designed, fabricated, and tested. The loads were implemented using metal patches with different lengths to modify the capacitance of the ring slot. This reflective surface provided reflection elevation angles of 22° ($\phi_R = 180°$) and 18° ($\phi_L = 0°$) at 32 GHz with axial ratios lower than 3 dB in the 31.01-32.69 GHz, and 30.98-32.91 GHz frequency bands for the RHCPW and LHCPW, respectively. The addition of varactor diodes to load the ring slots can be used to obtain an electronically reconfigurable MRS for reflectarray applications. The proposed approach can be suitable for the design of reconfigurable reflectarrays with dual circularly polarized waves to offer polarization diversity and beam scanning properties for the upcoming generation of wireless communication systems.

REFERENCES

[1] J. Huang and J. A. Encinar, *Reflectarray Antennas*. Hoboken, NJ, USA: Wiley, 2007.
[2] A. Moessinger, R. Marin, S. Mueller, J. Freese, and R. Jakoby, "Electronically reconfigurable reflectarrays with nematic liquid crystals," *Electron. Lett.*, vol. 42, no. 16, pp. 899–900, Aug. 2006.
[3] S. V. Hum, M. Okoniewski, and R. J. Davies, "Modeling and design of electronically tunable reflectarrays," *IEEE Trans. Antennas Propag.*, vol. 55, no. 8, pp. 2200–2210, Aug. 2007.
[4] J. Perruisseau-Carrier and A. K. Skrivervik, "Monolithic MEMS-based reflectarray cell digitally reconfigurable over a 360° phase range," *IEEE Antennas Wireless Propag. Lett.*, vol. 7, pp. 138–141, 2008.
[5] F. Venneri, S. Costanzo, and G. Di Massa, "Reconfigurable aperture-coupled reflectarray element tuned by single varactor diode," *Electron. Lett.*, vol. 48, no. 2, pp. 68–69, Jan. 2012.
[6] J. Rodriguez-Zamudio, J. I. Martinez-Lopez, J. Rodriguez-Cuevas, and A. E. Martynyuk, "Reconfigurable reflectarrays based on optimized spiraphase-type elements," *IEEE Trans. Antennas Propag.*, vol. 60, no. 4, pp. 1821–1830, Apr. 2012.
[7] E. Carrasco and J. Perruisseau-Carrier, "Reflectarray antenna at terahertz using graphene," *IEEE Antennas Wireless Propag. Lett.*, vol. 12, pp. 253–256, 2013.
[8] J. Han, L. Li, G. Liu, Z. Wu, and Y. Shi, "A wideband 1 bit 12 × 12 reconfigurable beam-scanning reflectarray: Design, fabrication, and measurement," *IEEE Antennas Wireless Propag. Lett.*, vol. 18, no. 6, pp. 1268–1272, Jun. 2019.
[9] X. Yang, S. Xu, F. Yang, M. Li, Y. Hou, S. Jiang, and L. Liu, "A broadband high-efficiency reconfigurable reflectarray antenna using mechanically rotational elements," *IEEE Trans. Antennas Propag.*, vol. 65, no. 8, pp. 3959–3966, Aug. 2017.
[10] T. Smith, U. Gothelf, O. S. Kim, and O. Breinbjerg, "Design, manufacturing, and testing of a 20/30-GHz dual-band circularly polarized reflectarray antenna," *IEEE Antennas Wireless Propag. Lett.*, vol. 12, pp. 1480–1483, 2013.
[11] M.-Y. Zhao, G.-Q. Zhang, X. Lei, J.-M. Wu, and J.-Y. Shang, "Design of new single-layer multiple-resonance broadband circularly polarized reflectarrays," *IEEE Antennas Wireless Propag. Lett.*, vol. 12, pp. 356–359, 2013.
[12] R. Deng, Y. Mao, S. Xu, and F. Yang, "A single-layer dual-band circularly polarized reflectarray with high aperture efficiency," *IEEE Trans. Antennas Propag.*, vol. 63, no. 7, pp. 3317–3320, Jul. 2015.
[13] M. K. T. Al-Nuaimi, A.-E. Mahmoud, W. Hong, and Y. He, "Design of single-layer circularly polarized reflectarray with efficient beam scanning," *IEEE Antennas Wireless Propag. Lett.*, vol. 19, no. 6, pp. 1002–1006, Jun. 2020.
[14] S. V. Hum and J. Perruisseau-Carrier, "Reconfigurable reflectarrays and array lenses for dynamic antenna beam control: A review," *IEEE Trans. Antennas Propag.*, vol. 62, no. 1, pp. 183–198, Jan. 2014.

[15] W. Tang, S. Mercader-Pellicer, G. Goussetis, H. Legay, and N. J. G. Fonseca, "Low-profile compact dual-band unit cell for polarizing surfaces operating in orthogonal polarizations," *IEEE Trans. Antennas Propag.*, vol. 65, no. 3, pp. 1472–1477, Mar. 2017.
[16] M. Zhou, S. B. Sørensen, N. Vesterdal, M. F. Palvig, Y. Brand, S. Maltais, J. Bellemore, and G. Toso, "Design of dual-band dual-polarized reflectarray for future multiple spot beam applications in Ka-band," in *Proc. 13th Eur. Conf. Antennas Propag. (EuCAP)*, Krakow, Poland, 2019, pp. 1–5.
[17] S. Mener, R. Gillard, R. Sauleau, A. Bellion, and P. Potier, "Dual circularly polarized reflectarray with independent control of polarizations," *IEEE Trans. Antennas Propag.*, vol. 63, no. 4, pp. 1877–1881, Apr. 2015.
[18] M.-A. Joyal, R. El Hani, M. Riel, Y. Demers, and J.-J. Laurin, "A reflectarray-based dual-surface reflector working in circular polarization," *IEEE Trans. Antennas Propag.*, vol. 63, no. 4, pp. 1306–1313, Apr. 2015.
[19] M. Hosseini and S. V. Hum, "A dual-CP reflectarray unit cell for realizing independently controlled beams for space applications," in *Proc. 11th Eur. Conf. Antennas Propag. (EUCAP)*, Paris, France, Mar. 2017, pp. 66–70.
[20] C. S. Geaney, M. Hosseini, and S. V. Hum, "Reflectarray antennas for independent dual linear and circular polarization control," *IEEE Trans. Antennas Propag.*, vol. 67, no. 9, pp. 5908–5918, Sep. 2019.
[21] P. Naseri, M. Riel, Y. Demers, and S. V. Hum, "A dual-band dual-circularly polarized reflectarray for K/Ka-band space applications," *IEEE Trans. Antennas Propag.*, vol. 68, no. 6, pp. 4627–4637, Jun. 2020.
[22] D. Martinez-de-Rioja, R. Florencio, J. A. Encinar, E. Carrasco, and R. R. Boix, "Dual-frequency reflectarray cell to provide opposite phase shift in dual circular polarization with application in multibeam satellite antennas," *IEEE Antennas Wireless Propag. Lett.*, vol. 18, no. 8, pp. 1591–1595, Aug. 2019.
[23] D. Martinez-de-Rioja, R. Florencio, E. Martinez-de-Rioja, M. Arrebola, J. A. Encinar, and R. R. Boix, "Dual-band reflectarray to generate two spaced beams in orthogonal circular polarization by variable rotation technique," *IEEE Trans. Antennas Propag.*, vol. 68, no. 6, pp. 4617–4626, Jun. 2020.
[24] X. Zhang, F. Yang, S. Xu, and M. Li, "Single-layer reflectarray antenna with independent dual-CP beam control," *IEEE Antennas Wireless Propag. Lett.*, vol. 19, no. 4, pp. 532–536, Apr. 2020.
[25] W.-L. Guo, G.-M. Wang, W.-Y. Ji, Y.-L. Zheng, K. Chen, and Y. Feng, "Broadband spin-decoupled metasurface for dual-circularly polarized reflector antenna design," *IEEE Trans. Antennas Propag.*, vol. 68, no. 5, pp. 3534–3543, May 2020.
[26] L. Martinez-Lopez, J. Rodriguez-Cuevas, J. I. Martinez-Lopez, and A. E. Martynyuk, "A multilayer circular polarizer based on bisected split-ring frequency selective surfaces," *IEEE Antennas Wireless Propag. Lett.*, vol. 13, pp. 153–156, 2014.
[27] N. Amitay, V. Galindo, and C. P. Wu, *Theory and Analysis of Phased Array Antennas*. New York, NY, USA: Wiley, 1972.

LOURDES MARTINEZ-LOPEZ was born in Mexico City, Mexico. She received the B.S., M.Eng., and Ph.D. degrees in electrical engineering from the National Autonomous University of Mexico (UNAM), Mexico City, in 2006, 2008, and 2015, respectively. She is currently a Professor of electrical engineering with UNAM. Her current research interests include circular polarizers, frequency selective surfaces, metasurfaces, and antenna arrays.

ROSALBA MARTINEZ-LOPEZ was born in Mexico City, Mexico. She received the B.S. degree in computer engineering, and the M.Eng. and Ph.D. degrees in electrical engineering from the National Autonomous University of Mexico (UNAM), Mexico City, in 2004, 2007, and 2013, respectively. Since 2013, she has been a Professor with the School of Engineering, UNAM. Her current research interests include frequency selective surfaces, micro-electromechanical systems (MEMS), antenna arrays, and microwave circuits.

JORGE RODRIGUEZ-CUEVAS was born in Mexico City, Mexico. He received the B.S., M.Eng., and Ph.D. degrees in electrical engineering from the National Autonomous University of Mexico (UNAM), Mexico City, in 1987, 1995, and 2003, respectively. In 2003, he received specialized studies in microelectromechanical systems (MEMS) from UNAM and the United States-Mexico Foundation for Science (FUMEC), Mexico City. Since 1987, he has been with the Electronics Engineering Department, UNAM, where he is currently a Professor involved in research and teaching on telecommunication circuits and systems. His current research interests are phased arrays, RF MEMS, and microwave and millimeter-wave circuits.

ALEXANDER E. MARTYNYUK was born in Kiev, Ukraine. He received the M.Sc. degree in radio engineering and the Ph.D. degree from the Kiev Polytechnic Institute, Kiev, in 1988 and 1993, respectively. From 1988 to 1995, he was with the Faculty of Radio Engineering, Kiev Polytechnic Institute. Since 1995, he has been with the National Autonomous University of Mexico (UNAM), Mexico City, Mexico. He is currently a Professor with the School of Engineering, UNAM. His research interests include microwave and millimeter-wave devices, antenna arrays, and millimeter-wave communications.

JOSE I. MARTINEZ-LOPEZ (Member, IEEE) was born in Mexico City, Mexico. He received the B.S., M.Eng., and Ph.D. degrees in electrical engineering from the National Autonomous University of Mexico (UNAM), Mexico City, in 1994, 1998, and 2005, respectively. In 2006, he was with the Schlumberger Technology Center, Sugar Land, TX, USA, where he was developing antennas for deep induction array tools for the oil industry. In 2009, he was a Visiting Scholar with the Electroscience Laboratory, The Ohio State University (OSU), Columbus, OH, USA. He is currently a Professor of electrical engineering with UNAM. He is also on a sabbatical leave as a Visiting Scholar with the Nonlinear RF Laboratory, Department of Electrical and Computer Engineering, ECE-OSU. His current research interests include antenna arrays, frequency selective surfaces, and microwave and millimeter-wave circuits.